photonics

MDPI

Article

Concentric-Ring-Assisted Multimode Fiber Supports Numerous High-Order LP Beams

Chengyang Zhu [1,2,3], Xi Zhang [4], Haixuan Xu [5], Jingwen Zhang [3], Shuqi Ma [6,*] and Yize Liang [1,2,*]

1 School of Optoelectronic Engineering, Xidian University, Xi'an 710071, China; zcy_2024@stu.xjtu.edu.cn
2 Modern Precision Measurement and Laser Non-Destructive Testing Key Laboratory of Higher Education in Fujian Province, PuTian University, Putian 351100, China
3 Key Laboratory for Physical Electronics and Devices of the Ministry of Education, School of Electronics Science and Engineering, Xi'an Jiaotong University, Xi'an 710049, China; jwzhang@xjtu.edu.cn
4 Jiangsu Alpha Optic-Electric Technology Co., Ltd., Suzhou 215200, China; zhangxi@jsalpha.com
5 China Mobile Information Technology Co., Ltd., Hangzhou 311100, China; xuhaixuan@cmhi.chinamobile.com
6 State Key Laboratory of Extreme Photonics and Instrumentation, College of Optical Science and Engineering, Zhejiang University, Hangzhou 310027, China
* Correspondence: msq@alumni.hust.edu.cn (S.M.); liangyize@xidian.edu.cn (Y.L.)

Abstract

This study proposes and numerically investigates the design and characterization of a ring-assisted (RA) fiber supporting 11 LP mode groups and a concentric-ring-assisted (CRA) fiber supporting 13 LP mode groups. Based on the relationship between the normalized frequency and the number of LP modes, a step-index (SI) fiber capable of supporting 13 LP mode groups is first designed. By leveraging the overlap between the high-index ring-assisted structure and the LP_{22} mode, the effective index difference (Δn_{eff}) between the LP_{22} and LP_{03} modes is enhanced. The resulting RA 11-LP mode fiber achieves a minimum effective index difference Min$|\Delta n_{eff}|$ of 0.78×10^{-3}, comparable to that of a standard SI 4-mode fiber, and a minimum effective area Min$|A_{eff}|$ of 164 μm^2, which effectively suppresses nonlinear effects. Furthermore, by introducing a second ring structure to form a CRA design, we realize a 13-LP mode fiber. This structure selectively increases the effective index of the LP_{61} mode through overlap with its power distribution, while leaving the effective index of the LP_{13} mode unaffected. The CRA 13-LP mode fiber exhibits highly stable effective indices across the C band. It demonstrates a Min$|\Delta n_{eff}|$ of 0.55×10^{-3}, which ensures effective mode separation and reduced inter-mode crosstalk. The Min$|A_{eff}|$ is 131 μm^2—still above 100 μm^2—thereby mitigating nonlinear impairments. With support for 46 spatial modes in total, this fiber significantly enhances transmission capacity.

Keywords: LP mode; few-mode fiber; fiber design; mode-division multiplexing

Check for updates

Received: 2 March 2026
Revised: 1 April 2026
Accepted: 6 April 2026
Published: 8 April 2026

Copyright: © 2026 by the authors. Licensee MDPI, Basel, Switzerland. This article is an open access article distributed under the terms and conditions of the Creative Commons Attribution (CC BY) license.

1. Introduction

With the advancement of optical communication, there is a growing demand for higher transmission capacity [1,2]. To address this, techniques such as polarization division multiplexing (PDM) [3], wavelength division multiplexing (WDM) [4], optical time-division multiplexing (OTDM) [5], and space-division multiplexing (SDM) [6–9] have been developed. As the first three approaches near full utilization, SDM has attracted significant attention for its potential to greatly improve communication within a single fiber [10–13]. Among SDM strategies, mode-division multiplexing (MDM) stands out for its ability to substantially increase capacity by enabling simultaneous transmission over multiple modes [14–22]. This

has also spurred the development of multi-input multi-output (MIMO) technology [23–25]. However, as the number of modes increases, so do the cost and complexity of MIMO-based digital signal processing.

MDM has been widely implemented using weakly coupled step-index few-mode fibers (SI-FMFs), which reduce reliance on MIMO processing [26–30]. Studies have shown that increasing the effective index difference (Δn_{eff}) between modes can effectively suppress inter-mode crosstalk (IM-XT) [31–33]. For instance, SI-FMFs supporting four LP modes have been successfully fabricated, enabling 100 Gbps transmission over two degenerate LP_{11} modes across 40 km [34]. These fibers exhibit a minimum effective index difference ($Min|\Delta n_{eff}|$) of 0.8×10^{-3}, allowing error-free decoding after 40 km of transmission. Ring-assisted (RA) structures offer several advantages, including relatively weak mode coupling among high-order azimuthal modes, which simplifies digital signal processing; a large effective area to mitigate nonlinear effects; and theoretically uniform optical amplifier gain across modes [35–39].

Previous studies have indicated that increasing the inter-modal effective index gap can enhance mode separation and reduce coupling, thereby improving transmission stability [40–43]. It has been demonstrated that ring-assisted fibers supporting four LP modes can achieve a minimum effective index difference ($Min|\Delta n_{eff}|$) as high as 1.8×10^{-3}, which significantly suppresses IM-XT [44]. Experimental results confirm that the high-index ring maintains signal integrity without additional distortions. These findings underscore the effectiveness of RA structures in strategically controlling refractive index distributions [45,46]. By utilizing multiple ring-assisted regions or ellipse-assisted designs [46], it becomes feasible to support a greater number of LP or OAM modes, significantly enhancing transmission capacity [47,48]. Although current RA fibers generally support limited spatial modes, advanced designs—including graded-index ring-core and W-type structures—are essential to further scale mode density and improve bandwidth in future optical communication systems [48,49].

In this paper, we present the design and characterization of an RA fiber supporting 11 LP mode groups and a CRA fiber supporting 13 LP mode groups. To ensure sufficient mode support, we used the normalized propagation constant and a normalized frequency to determine fiber parameters capable of sustaining 13 LP mode groups. The high-index ring-assisted structure is then employed to selectively adjust modal effective indices. By optimizing the overlap between the RA structure and the LP_{22} mode's power profile, the effective index of LP_{22} is raised while that of LP_{03} remains largely unaffected. Compared to a conventional SI four-mode fiber, the proposed RA structure maintains a similar $Min|\Delta n_{eff}|$ of 0.78×10^{-3} and a $Min|A_{eff}|$ of 164 μm^2, effectively curbing nonlinearity while significantly increasing the number of modes.

Building on this, a second high-index ring is introduced to form a CRA structure. Through overlap with the power distribution of the LP_{61} mode, its effective index is increased without affecting the LP_{13} mode, thereby realizing a 13-LP mode fiber. The CRA fiber exhibits highly stable effective indices across the C band, with a $Min|\Delta n_{eff}|$ of 0.55×10^{-3} and a $Min|A_{eff}|$ of 131 μm^2. It successfully supports 13 LP mode groups, substantially improving fiber transmission capacity.

2. Design Principle and Approach

In multimode optical fibers, mode coupling often occurs, leading to scattering losses. To minimize the mode coupling coefficient, the expression for this coefficient is given as follows:

$$K_{pq} = \frac{\omega\varepsilon_0\left(n_{core}^2 - n_{clad}^2\right)a}{4iP}\int_0^{2\pi} \boldsymbol{E_p^*}(a)\cdot\boldsymbol{E_q}(a)f(z)\cos(m\phi+\psi)d\phi = f(z)\overline{K_{pq}}, \quad (1)$$

where ω is angular frequency, ε_0 is vacuum permittivity, n_{core} is the core refractive of a vacuum, n_{clad} is the cladding refractive of a vacuum, a is the radius of the core, P is the optical power, and $\boldsymbol{E}_{\boldsymbol{p}}^{*}(a)$ and $\boldsymbol{E}_{\boldsymbol{q}}(a)$ represent the optical field of different modes at the core–cladding interface. $f(z)\cos(m\phi + \psi)$ is the fluctuation compared with the ideal waveguide. $\overline{K_{pq}}$ is the geometric factor related to the spatial distribution of mode fields and fiber deformation. The power coupling coefficient can be expressed as the following:

$$h_{pq} = \left|\overline{K_{pq}}\right|^2 F(\Delta\beta_{pq}), \tag{2}$$

where $F(\Delta\beta_{pq})$ is the power spectrum density of $f(z)$ at frequency $\Delta\beta_{pq}$. h_{pq} depends on Δn_{eff} or on the micro-bends. For FMFs, there is a threshold point called Δn_{eff}^{th}. When $\Delta n_{eff} < \Delta n_{eff}^{th}$, h_{pq} decreases with the increase in Δn_{eff}. When $\Delta n_{eff} > \Delta n_{eff}^{th}$, h_{pq} is approximated by a constant. The numerical value of h_{pq} is often limited by the intrinsic distortions in the manufacturing process. When FMFs are subjected to significant winding tension, a higher Δn_{eff} is required to suppress the h_{pq} between modes. Consequently, to mitigate the adverse effects of random perturbations while expanding the mode-supporting capacity, it is critical to maximize Δn_{eff} during the fiber design process to ensure robust modal isolation.

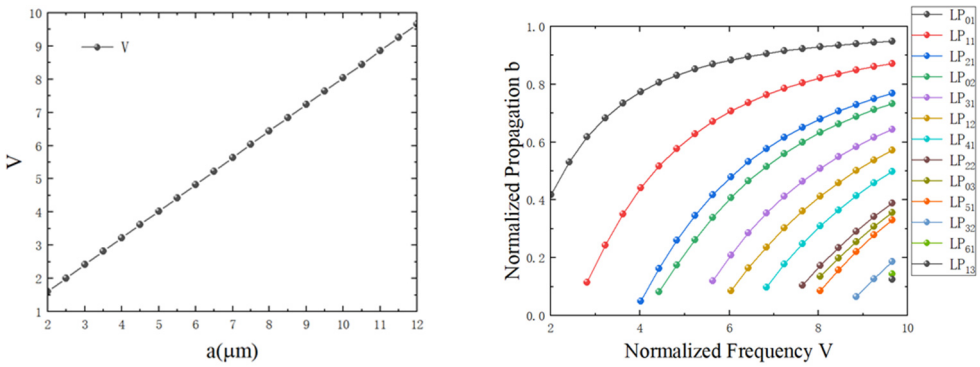
In the fiber design process, it is essential to first define the core radius and the refractive index of the cladding as foundational parameters. In the design of SI fibers, the normalized propagation constant b and the normalized frequency V are employed as key parameters to characterize the modal behavior. These two parameters are defined by the following expressions:

$$V = 2\pi a\sqrt{n_{core}^2 - n_{clad}^2}/\lambda \tag{3}$$

$$b = (n_{eff}^2 - n_{clad}^2)/(n_{core}^2 - n_{clad}^2), \tag{4}$$

where λ is the wavelength and n_{eff} is the effective refractive of a vacuum. To elucidate the relationship between the core radius a and the normalized frequency V, the variation of b as a function of V is illustrated in Figure 1a. Furthermore, to maximize the supported LP mode count, the evolution of the modes in the SI-FMF is analyzed by adjusting V and the propagation constant b, with the results presented in Figure 1b. As illustrated in Figure 1a, the stability of the normalized frequency V improves as the core radius a increases. Furthermore, Figure 1b reveals that the LP_{61} and LP_{13} modes emerge only when the V value reaches a specific threshold of 9.653699, marking the transition point for these higher-order modes in the SI-FMF. A Δn_{core} of less than 1% is specifically targeted to ensure fabrication feasibility. Exceeding this threshold significantly degrades manufacturing tolerance due to increased internal stress and potential preform cracking in standard MCVD/VAD processes. Within this 1% limit, our parametric scanning reveals that the selected values provide the optimal trade-off between mode capacity and modal separation.

To enable the fiber to support modes LP_{61} and LP_{31}, the core parameters are optimized with a Δn_{core} of 0.94% and an r_{core} of 11.6 μm. It is observed that three specific sets of LP modes exhibit a highly degenerate propagation constant b, namely LP_{22} and LP_{03} modes, as well as LP_{03} and LP_{51} modes, and LP_{61} and LP_{31} modes. Increasing the Δn_{eff} between these nearly degenerate pairs—particularly the LP_{22} and LP_{03} modes, and the LP_{61} and LP_{31} modes—is crucial for minimizing IM-XT and enhancing the overall transmission performance. Generally, a larger numerical aperture is preferred in SI-FMFs to achieve a higher Δn_{eff}, thereby effectively suppressing IM-XT.



(**a**) (**b**)

Figure 1. (**a**) The relationship between a and normalized frequency V. (**b**) Changing the normalized propagation constant b and the normalized frequency V changes the mode in the SI-FMF.

To quantitatively evaluate the nonlinear tolerance of the proposed structure for high-power transmission, the nonlinear coefficient γ is introduced and defined as the following:

$$\gamma = \frac{2\pi n_{SiO_2}}{\lambda A_{eff}}, \tag{5}$$

where n_{SiO_2} is the nonlinear refractive index of silicon dioxide (2.4×10^{-20} m^2/W) and A_{eff} is the effective mode area. As indicated by the equation, a larger A_{eff} effectively scales down the nonlinear coefficient, thereby suppressing Kerr-induced impairments such as self-phase modulation (SPM) and cross-phase modulation (XPM) in long-haul transmission systems.

In this work, the Δn_{eff} and the walk-off length are adopted to evaluate the influence of fiber bending on the eigenmodes within the ring regions. $L_{2\pi}$ and L_{10ps} represent the propagation length when the x and y LP mode in the fiber have a 2π relative phase shift and a 10-ps temporal walk off. It is given by the following equations:

$$L_{2\pi} = \frac{\lambda}{n_{eff}^x - n_{eff}^y} \tag{6}$$

$$L_{10ps} = \frac{c \times \Delta t}{n_{eff}^x - n_{eff}^y A}, \tag{7}$$

where λ, c, and Δt symbolize the wavelength, the vacuum velocity of light, and the temporal walk-off time, respectively. These parameters are fundamental in determining the modal characterization lengths, ensuring the scaling consistency between the phase-matching properties and the temporal walk-off limits.

Integrating a ring-assisted (RA) structure into a step-index (SI) FMF provides an effective mechanism for redistributing the modal effective indices. By strategically overlapping the high-index RA region with specific modal fields, the phase constants of targeted modes can be selectively modulated. As illustrated in Figure 2a,b, the first RA structure exhibits a high spatial overlap with the LP_{22} mode but significantly less overlap with the LP_{03} mode. This selective overlap increases the n_{eff} of LP_{22} while leaving LP_{03} relatively unaffected, thereby widening their effective index difference. Specifically, the first ring is optimized to separate the LP_{22}–LP_{03} pair, while the second ring is strategically positioned to enhance the separation between the LP_{61}–LP_{13} pair. These two pairs are prioritized because their similar radial field distributions and closely matched n_{eff} in standard step–index fibers represent the primary limiting factors for Min $|\Delta n_{eff}|$. By fine-tuning the width, radial position, and refractive index profile of these rings, we can effectively redistribute the n_{eff} of specific

high-order modes, ensuring that all 13 LP mode groups satisfy the Min $|\Delta n_{eff}| > 1 \times 10^{-4}$ criterion for low-crosstalk transmission.

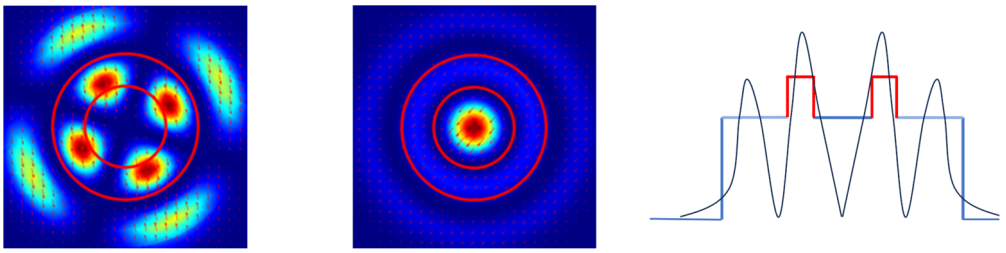


Figure 2. (**a**) Mode distribution of the LP_{22} mode; (**b**) mode distribution of the LP_{03} mode in RA-FMF; (**c**) overlap between the RA structure and the LP_{22} mode.

Initially, the SI fiber parameters (Δn_{core} = 0.94%, r_{core} = 11.6 μm) that support the LP_{61} and LP_{31} modes are selected as the baseline model for this study. Subsequently, the finite element simulation implemented in COMSOL Multiphysics 6.1 is employed to numerically investigate how various structural parameters of the RA configuration influence the fiber's modal characteristics. As shown in Figure 3a, the yellow ring is a high refractive index ring. In Figure 3b, W_{ring1} is the width of the high refractive index ring 1, Δn_1^+ is the refractive index difference between the high refractive index ring and the core layer, and R_{in_ring1} is the radius of the inner circle of ring 1. We use $\Delta n_1^+ = n_{ring1} - n_{core}$ to express the difference between the refractive index of the high refractive index ring 1 and the refractive index of the core layer. The selection of the experimental initial values of Δn_1^+, R_{in_ring1}, and W_{ring1} considered the feasibility of the preparation process and the mode operation of the RA 11-LP mode fiber.

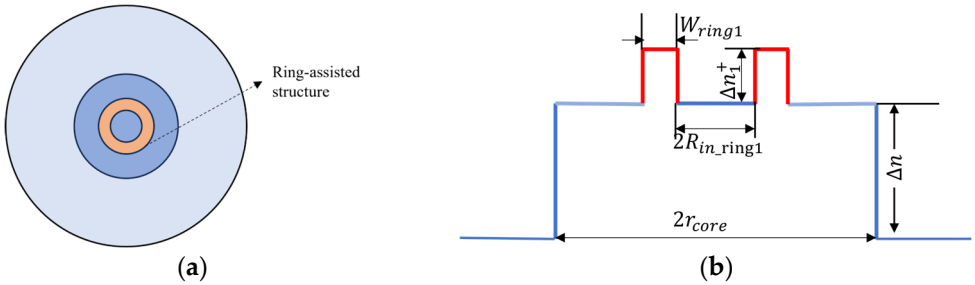


Figure 3. (**a**) Cross-sectional diagram of the RA 11-LP mode fiber. (**b**) Refractive index profile of the RA 11-LP mode fiber.

At the operating wavelength of 1550 nm, the dependence of n_{eff} on the structural parameters of the first RA structure (Δn_1^+, R_{in_ring1}, and W_{ring1}) is systematically analyzed in Figure 4. It is observed that in the foundational fiber profile, the Δn_{eff} between the LP_{13} and LP_{61} modes remains the primary bottleneck due to their closely matched phase constants, which necessitates the introduction of the second RA structure to achieve a robust 13-LP-mode-group fiber.

As illustrated in Figure 4a, with W_{ring1} and R_{in_ring1} held constant, the Δn_{eff} between LP_{13} and LP_{61} increases monotonically with the doping concentration (Δn_1^+). However, an excessive refractive index difference (exceeding 0.2%) induces a "mode compression" effect, where the Δn_{eff} for the LP_{31}–LP_{12} and LP_{41}–LP_{22} pairs begins to deteriorate. This trade-off suggests that the index perturbation must be carefully constrained to maintain global modal isolation. The radial position R_{in_ring1} also plays a critical role in selective modal field enhancement. As shown in Figure 4b, deviations from the optimal range (3.5 μm to 4.5 μm) lead to an abrupt decline in Δn_{eff} for several adjacent mode pairs, as

the ring structure shifts away from the high-field regions of the targeted modes. Similarly, Figure 4c indicates that while increasing the ring width W_{ring1} generally enhances modal separation, a range of 2.75 μm to 3.5 μm provides the most stable performance.

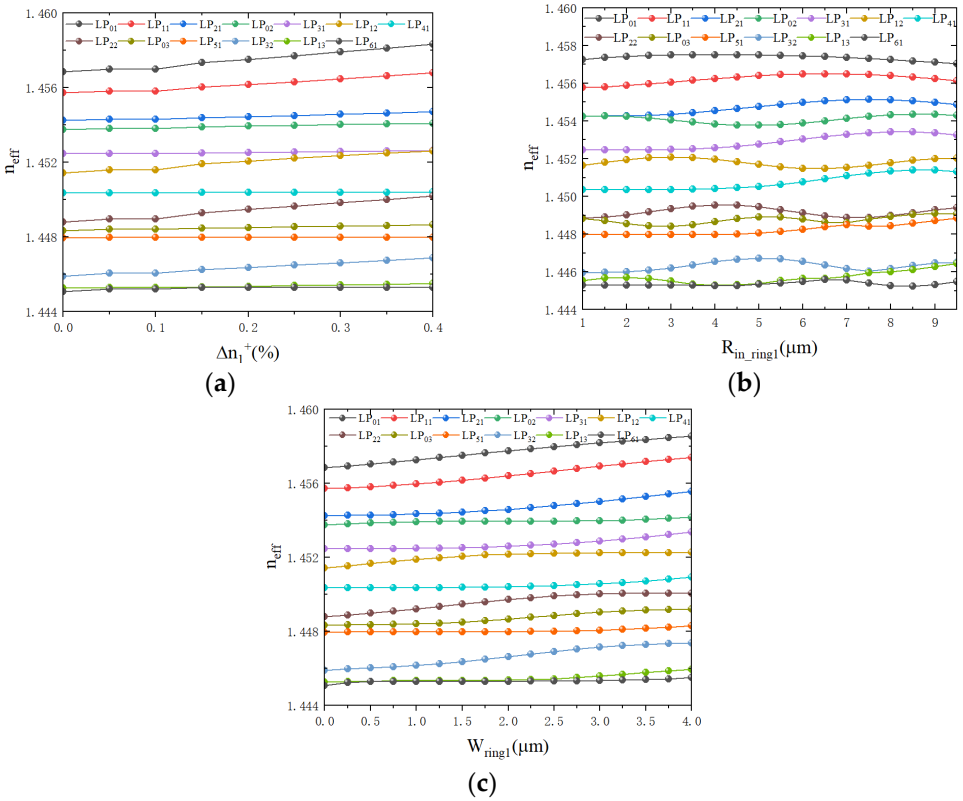


Figure 4. The RA 11-LP mode fiber with Δn_{core} = 0.94% and r_{core} = 11.6 μm as a function of (**a**) the first ring-core index difference Δn, with W_{ring1} = 1.5 μm and R_{in_ring1} = 3.5 μm; (**b**) the radius of the inner circle of the ring 1 R_{in_ring1}, with W_{ring1} = 1.5 μm and Δn_1^+ = 0.2%; (**c**) the width of the high refractive index ring 1 W_{ring1}, with R_{in_ring1} = 3.5 μm and Δn_1^+ = 0.2%.

Because any structural modification induces localized perturbations that affect the entire eigenvalue spectrum of the fiber, a multi-parameter synergistic optimization strategy was employed. We focused on the simultaneous adjustment of (R_{in_ring1}, Δn_1^+) and (R_{in_ring1}, W_{ring1}) to identify the global "sweet spot" that maximizes the Min | Δn_{eff} | . This approach ensures that even the most sensitive high-order modes, such as LP_{32} and LP_{13}, maintain sufficient separation to suppress inter-mode power transfer.

3. Mode Characteristics of the RA 11-LP Mode Fiber

Based on the above analysis, we micro-adjusted the parameters of the RA structure to determine the range of parameters that can achieve the maximum Min | Δn_{eff} | around Δn_1^+ = 0.19% and W_{ring1} = 3.1 μm. Therefore, we use different symbols to represent different Δn_1^+ and W_{ring1} in Figure 5, and greatly change the value of R_{in_ring1} to find the best RA structure. The Δn_{eff} of the six adjacent LP modes selected in Figure 5 is greatly affected by the RA structure and may become Min | Δn_{eff} | .

To validate the design's robustness, a quantitative sensitivity analysis was performed for the RA-FMF (Figure 5). Based on the bottleneck mode pair LP_{41}–LP_{02}, the following sensitivities were identified: a 0.1 μm increase in R_{in_ring1} results in Δn_{eff} shifts of $+0.01 \times 10^{-3}$ and -0.04×10^{-3} for the LP_{41}–LP_{22} and LP_{22}–LP_{03} pairs, respectively. Similarly, a 0.1 μm enhancement in W_{ring1} leads to variations of $+0.01 \times 10^{-3}$ (LP_{41}–LP_{22}) and -0.001×10^{-3} (LP_{22}–LP_{03}). Furthermore, the impact of the Δn_1^+ is non-linear; each 0.01% increment induces

Δn_{eff} shifts ranging from $+0.01 \times 10^{-3}$ to $+0.05 \times 10^{-3}$ for LP_{41}–LP_{22} and -0.002×10^{-3} to -0.04×10^{-3} for LP_{22}–LP_{03}, with the sensitivity intensifying at higher baseline doping levels. It is worth highlighting that even under these parameter fluctuations, this specific mode pair remains the critical bottleneck, consistently exhibiting the minimum effective refractive index difference across the entire supported mode spectrum.

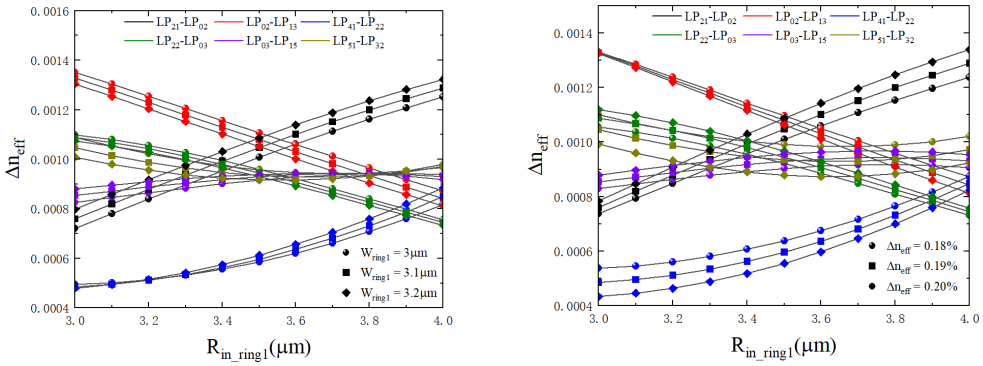


Figure 5. When the RA 11–LP mode fiber is under the condition of Δn_{core} = 0.94%, r_{core} = 11.6 μm, and W_{ring1} = 3.1 μm. (**a**) Δn_{eff} as a function of R_{in_ring1} and Δn_1^+; (**b**) Δn_{eff} as a function of R_{in_ring1} and W_{ring1}.

Therefore, the best structural parameters of RA 11-LP mode fiber are R_{in_ring1} = 3.9 μm, Δn_1^+ = 0.19%, and W_{ring1} = 3.1 μm. The maximum $\mathrm{Min}|\Delta n_{eff}|$ = 0.78 × 10^{-3} can be achieved, which is the same as that of SI-FMF.

The main characteristics of the optimized RA 11-LP mode fiber at 1550 nm are listed in Table 1. The $\mathrm{Min}|A_{eff}|$ of the RA 11-LP mode fiber is 164 μm^2, and more than 100 μm^2 can effectively reduce the influence of optical nonlinearity. The calculated nonlinear coefficient γ of the proposed fiber is approximately 0.593 $W^{-1} \times km^{-1}$ at 1550 nm, which is significantly lower than that of conventional few-mode fibers (typically > 1.1 $W^{-1} \times km^{-1}$). This 46% reduction in nonlinearity is attributed to the large effective area. DGD vs. LP_{01} is the mode group delay relative to the LP_{01} mode, and the delay of the 11 LP mode groups supported by the fiber is not large. As the number of LP modes supported by the fiber increases, the dispersion will gradually increase; however, it is basically below 40 ps/(nm × km). Since the data is mainly obtained by simulation, the basic order of magnitude of the limiting loss is 10^{-12} dB/km, which is far less than 10^{-7} dB/km. Therefore, the simulation results can be considered up to standard.

Table 1. Characteristics of the optimized RA 11-LP mode fiber at 1550 nm.

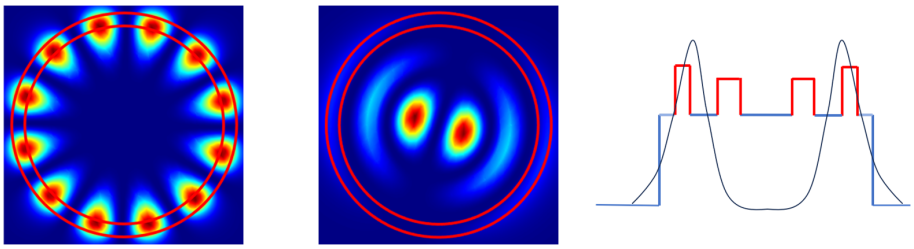
	LP_{01}	LP_{11}	LP_{21}	LP_{02}	LP_{31}	LP_{12}	LP_{41}
$n_{eff}(\times 1)$	1.4581	1.4570	1.4552	1.4539	1.4530	1.4521	1.4507
$\mathrm{Min}\lvert\Delta n_{eff}\rvert(\times 10^{-3})$				0.78			
A_{eff} μm^2	231	180	209	211	229	228	232
DGD vs. LP_{01} (ps/m)		3.8	9.8	13.9	16.9	20.2	24.8
Dispersion [ps/(nm·km)]	11.68	18.54	12.91	19.41	11.46	24.75	8.32
Limited Loss (10^{-12} dB/km)	0.282	0.247	0.0088	1.387	0.112	0.257	0.0804
	LP_{22}	LP_{03}		LP_{51}		LP_{32}	
$n_{eff}(\times 1)$	1.4499	1.4491		1.4481		1.4472	
$\mathrm{Min}\lvert\Delta n_{eff}\rvert(\times 10^{-3})$				0.78			
A_{eff} μm^2	235	164		229		237	
DGD vs. LP_{01} (ps/m)	27.4	30.0		33.3		36.5	
Dispersion [ps/(nm·km)]	35.96	9.7		10.1		15.88	
Limited Loss (10^{-12} dB/km)	0.138	1.069		0.0053		0.339	

The high baseline Δn_{eff} of the optimized first ring acts as a robust barrier, as the index fluctuations induced by environmental perturbations (10^{-5}) are several orders of magnitude smaller than the engineered modal gap [50]. Consequently, the design maintains stable mode separation and low crosstalk even under the mechanical stresses and thermal variations encountered in practical deployment [51]. Notably, the design exhibits significant robustness against fabrication tolerances. Specifically, given the substantial baseline Δn_{eff} of 0.78×10^{-3}, the fiber maintains a nearly eight-fold safety margin above the critical threshold 10^{-4} required for stable mode isolation. This ensures that minor geometric variations in the core radius or ring thickness during manufacturing do not compromise the low-crosstalk performance.

4. Design, Characterization, and Comparative Analysis of the 13-LP Mode Fiber

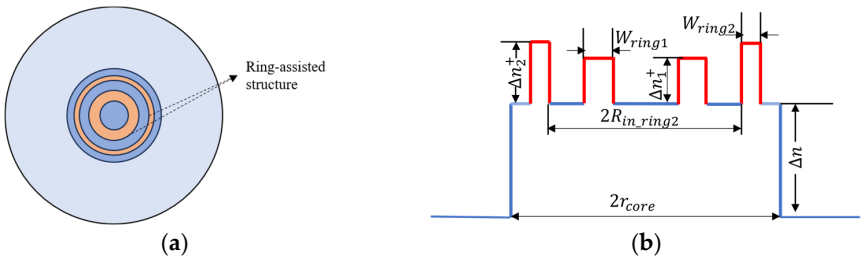
4.1. Design of the CRA 13-LP Mode Fiber

Based on the above method, we designed the second RA structure to separate the LP_{61} and LP_{13} modes. As illustrated in Figure 6a,b, the second RA structure is highly overlapped with the LP_{61} mode and weakly overlapped with the LP_{31} mode, which increases the Δn_{eff} between LP_{61} and LP_{13}. The overlap between the second RA structure and the LP_{61} mode is shown in Figure 6c. Figure 7a shows the schematic diagram of the fiber with a concentric ring structure. In Figure 7b, W_{ring2} is the width of the high refractive index ring 2, Δn_2^+ is the refractive index difference between the high refractive index ring 2 and the core layer, and R_{in_ring2} is the radius of the inner circle of ring 2. We use $\Delta n_2^+ = n_{ring2} - n_{core}$ to express the difference between the refractive index of the high refractive index ring 1 and the refractive index of the core layer. The two RA structures have the same center of the circle, which is called the CRA 13-LP mode fiber.



(**a**) (**b**) (**c**)

Figure 6. (**a**) Mode distribution of the LP_{61} mode; (**b**) mode distribution of the LP_{31} mode in the CRA 13-LP mode fiber; (**c**) overlap between the RA structure and the LP_{61} mode.



(**a**) (**b**)

Figure 7. (**a**) Cross-sectional diagram of the CRA 13-LP mode fiber. (**b**) Refractive index profile of the CRA 13-LP mode fiber.

Notably, the structural dimensions of the second RA ring are strictly constrained by the radial distributions of the targeted high-order modes. The inner and outer radii are optimized at 9.9 μm and 11.2 μm, respectively, to ensure precise modal control. If the inner boundary is less than 9.9 μm, the RA structure incurs an unintended spatial overlap

with the LP_{51} mode, which excessively elevates its n_{eff} and consequently reduces the Δn_{eff} between the LP_{51} and LP_{03} pair. Conversely, if the outer boundary fails to reach 11.2 μm, the LP_{61} mode—which exhibits a more extended radial field—will experience insufficient overlap with the high-index region. This results in a negligible shift in its n_{eff}, rendering the RA structure ineffective for separating the LP_{61}–LP_{13} mode pair. Therefore, this specific radial window serves as a spatial filter that selectively modulates the phase constants of target modes while preserving the isolation of adjacent mode groups.

Based on the previous parameters of the first RA structure, the second RA structure parameter scan is performed. Since the outer boundary of the first RA structure is 6.6 μm, R_{in_ring2} chooses to start from 7 μm. Under the condition of light with a wavelength of 1550 nm, the function of n_{eff} with Δn_2^+, R_{in_ring2}, and W_{ring2} is shown in Figure 8a–c. By observing Figure 8a, it is found that with an increase in Δn_2^+, the Δn_{eff} between LP_{61} and LP_{31} modes does not increase significantly and remains almost unchanged. As illustrated in Figure 8b, it is found that when R_{in_ring2} is greater than 7.5 μm, the Δn_{eff} of LP_{61} and LP_{31} modes gradually increases, and when it exceeds 9.25 μm, it gradually decreases. In this interval, the Δn_{eff} of the LP_{03} and LP_{51} modes is too small, and the effect is not ideal. As illustrated in Figure 8c, with an increase in W_{ring2}, and when W_{ring2} is greater than 2.25 μm, the Δn_{eff} of LP_{61} and LP_{31} modes gradually increases. However, the Δn_{eff} of LP_{32} and LP_{61} gradually decreases, which means that the best result is not in this range. Therefore, the radial position of the first RA structure must be adjusted, while the second ring should be strategically spaced from the first to minimize cross-modal interference.

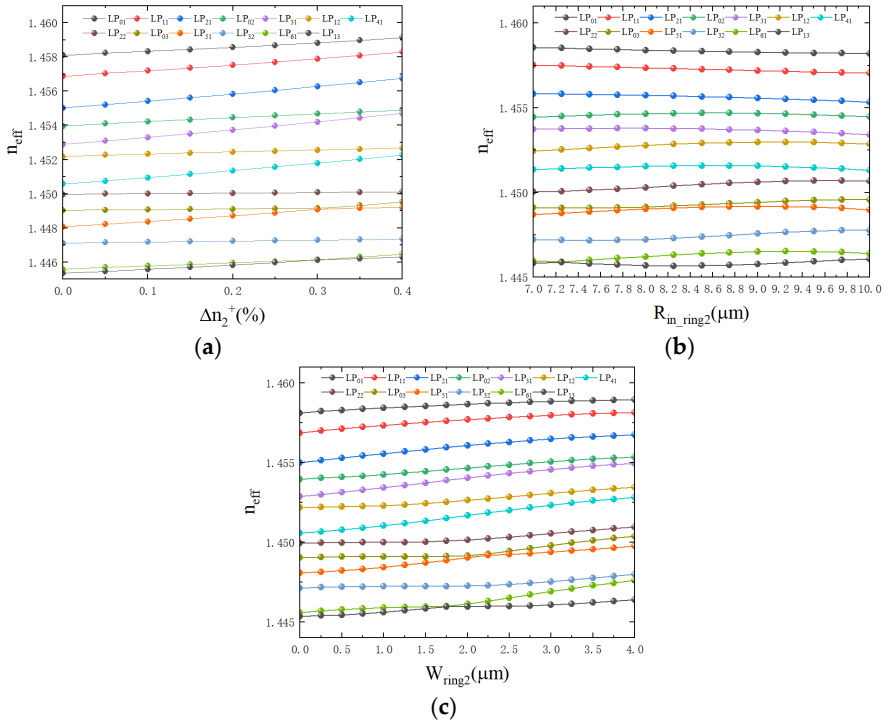
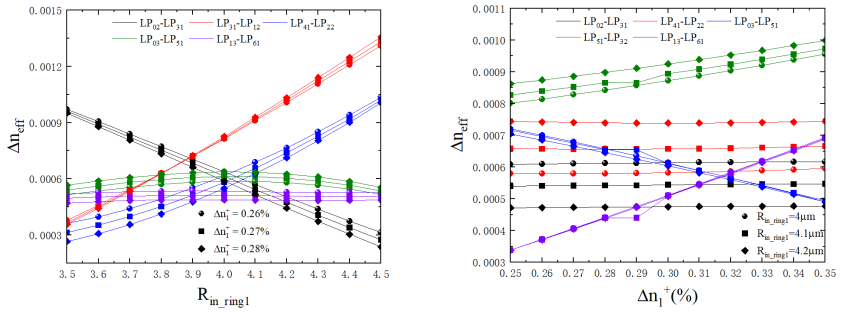


Figure 8. CRA 13-LP mode fiber with Δn_{core} = 0.94%, r_{core} = 11.6 μm, R_{in_ring1} = 3.9 μm, Δn_1^+ = 0.19%, and W_{ring1} = 3.1 μm as a function of (**a**) the second ring-core index difference Δn_2^+ with W_{ring2} = 1.5 μm and R_{in_ring2} = 7 μm; (**b**) the radius of the inner circle of the ring 2 R_{in_ring2} with W_{ring2} = 1.5 μm and Δn_2^+ = 0.2%; (**c**) the width of the high refractive index ring 2 W_{ring2} with R_{in_ring2} = 7 μm and Δn_2^+ = 0.2%.

To pinpoint the optimal design, a systematic evaluation was conducted. As shown in Figure 9a, within the identified optimal regime, the Δn_{eff} of LP_{31}–LP_{12} and LP_{41}–LP_{22} improves with R_{in_ring1}, while LP_{02}–LP_{31} exhibits the opposite trend. Building upon this,

a fine-grained optimization was performed by coupling Δn_1^+ and R_{in_ring1} (Figure 9b) to maximize the global Min | Δn_{eff} |. Based on this baseline, a quantitative sensitivity analysis was performed for the CRA-FMF. For the first RA structure, a 0.1 μm increase in R_{in_ring1} results in Δn_{eff} variations of $+0.005 \times 10^{-3}$, $+0.04 \times 10^{-3}$, and -0.07×10^{-3} for the LP_{31}–LP_{61}, LP_{41}–LP_{22}, and LP_{02}–LP_{21} pairs, respectively. Similarly, each 0.01% increment in Δn_1^+ leads to shifts of -0.05×10^{-3} (LP_{41}–LP_{22}), -0.01×10^{-3} (LP_{02}–LP_{21}), and -0.025×10^{-3} (LP_{31}–LP_{61}). Crucially, this mode pair remains the limiting bottleneck with the Min | Δn_{eff} | across the analyzed range. Optimal parameters for the first ring of the CRA structure were identified as follows: R_{in_ring1} = 4.1 μm, W_{ring1} = 3.1 μm, and Δn_1^+ = 0.27%.



(**a**) (**b**)

Figure 9. When CRA 13-LP mode fiber is under the condition of Δn_{core} = 0.94%, r_{core} = 11.6 μm, W_{ring1} = 3.1 μm, R_{in_ring2} = 9.9 μm, W_{ring2} = 1.3 μm, and Δn_2^+ = 0.3%. (**a**) Δn_{eff} as a function of the coarse-stepped R_{in_ring1} and the fine-stepped Δn_1^+; (**b**) Δn_{eff} as a function of the fine-stepped R_{in_ring1} and the coarse-stepped Δn_1^+.

The simulation of R_{in_ring2} and Δn_2^+ of the second RA structure is carried out on the identified first RA structure. The outer ring of the second RA structure is fixed at 11.2 μm, and the Δn_2^+ and W_{ring2} are changed as shown in Figure 10. With an increase in Δn_2^+ and the Δn_{eff} of the LP_{51} and LP_{32} modes, the LP_{13} and LP_{61} modes increase, the Δn_{eff} of the LP_{03} and LP_{51} modes decrease, and the Δn_{eff} of the other two groups is almost unchanged. Therefore, the best parameter of the second RA structure is Δn_2^+ = 0.32% and W_{ring2} = 1.3 μm. To validate the robustness of this design, a quantitative sensitivity analysis was performed around this optimal point. A 0.1 μm increase in W_{ring2} results in Δn_{eff} shifts of $+0.013 \times 10^{-3}$ and -0.0015×10^{-3} for the LP_{31}–LP_{61} and LP_{02}–LP_{21} pairs, respectively. Furthermore, for every 0.01% increment in Δn_2^+, the Δn_{eff} for LP_{02}–LP_{21} and LP_{31}–LP_{61} varies by $+0.001 \times 10^{-3}$ and $+0.03 \times 10^{-3}$. In all cases, this mode pair persists as the critical bottleneck, consistently exhibiting the lowest Δn_{eff} across the investigated parameter range.

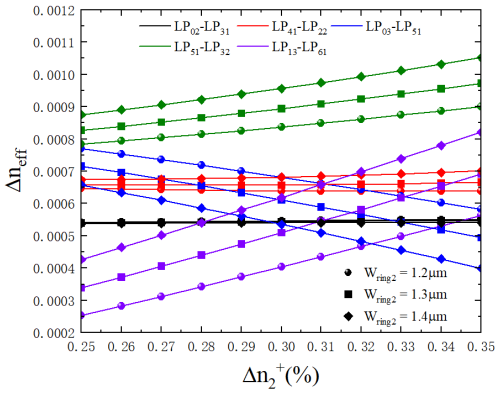


Figure 10. When the CRA 13-LP mode fiber is under the condition of Δn_{core} = 0.94%, r_{core} = 11.6 μm, R_{in_ring1} =4.1 μm, W_{ring1} = 3.1 μm, and Δn_1^+ = 0.27%. Δn_{eff} as a function of Δn_2^+ and W_{ring2}.

4.2. Mode Characteristics of the CRA 13-Mode Fiber

Figure 11 is a schematic diagram of all the modes supported by the CRA 13-LP mode fiber at a wavelength of 1550 nm. The LP_{0n} mode is two-fold degenerate, whereas the other LP modes are quadruple degenerate. In Figure 11, x and y of the LP mode represent the polarization direction, and a and b represent two mutually orthogonal modes. We also measured the n_{eff} of the CRA 13-LP mode fiber at different wavelengths. As illustrated in Figure 12, the n_{eff} of all supported modes remains remarkably stable across the entire C band. The negligible fluctuations in n_{eff} with respect to wavelength variations demonstrate that the modal characteristics are highly insensitive to wavelength changes, ensuring consistent performance over a broad operating range.

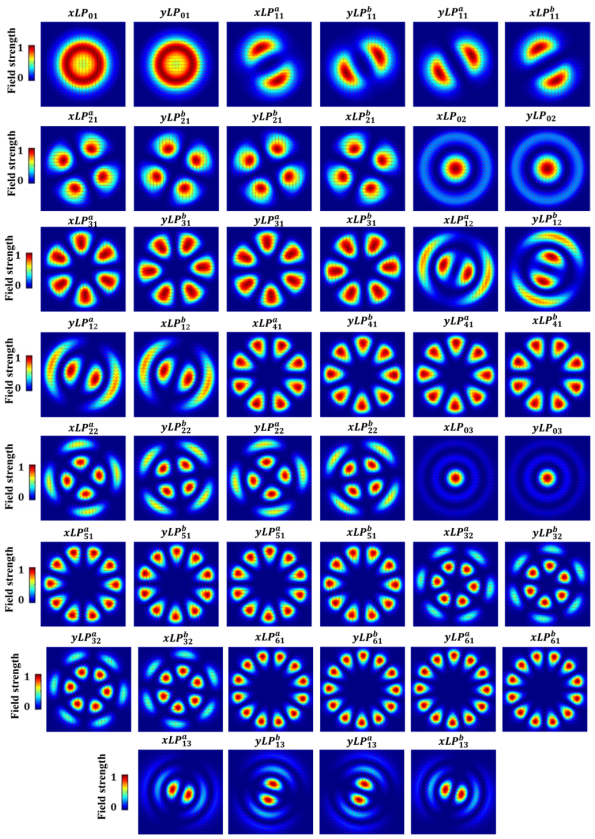


Figure 11. A schematic diagram of all the modes supported by the CRA 13-LP mode fiber at a wavelength of 1550 nm.

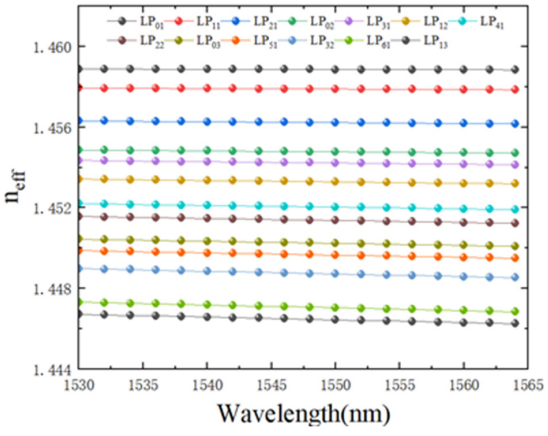


Figure 12. Effective refractive index of all the LP modes of the CRA 13-LP mode fiber within the C band.

Figure 13a,b illustrate the Δn_{eff}, $\mathbf{L_{2\pi}}$, and $\mathbf{L_{10ps}}$ under varying bending radii at λ = 1550 nm. For lower-order modes such as LP_{01} and LP_{21}, the Δn_{eff} exhibits significant variations from 10^{-6} to 10^{-9} as the bending radius increases from 1 cm to 100 cm. In contrast, higher-order modes like LP_{61} and LP_{13} show a larger variation in range, with Δn_{eff} spanning from 10^{-3} to 10^{-6}. At a tight bending radius of approximately 1 cm, the $\mathbf{L_{2\pi}}$ and $\mathbf{L_{10ps}}$ for higher-order modes are markedly reduced, but they significantly improve and stabilize once the radius exceeds 5 cm. Most modes reach a steady state beyond a 10 cm radius, with negligible changes in $\mathbf{L_{2\pi}}$ and $\mathbf{L_{10ps}}$ between 50 cm and 100 cm. For bending radii above 5 cm, the $\mathbf{L_{10ps}}$ of higher-order modes reaches several hundred meters, while lower-order modes can achieve 10^5 m to 10^6 m, with the LP_{01} mode even reaching 10^7 m. Crucially, the identified bottleneck mode pair consistently maintains the Min | Δn_{eff} | throughout the bending analysis, effectively suppressing inter-mode crosstalk under realistic physical perturbations. This high modal isolation allows for modular, small-scale MIMO equalization within mode groups instead of high-complexity global MIMO, significantly reducing computational overhead. Consequently, the proposed CRA-FMF is well-suited for stable short-to-medium haul transmissions (e.g., data center interconnects) where low-complexity signal processing and robust crosstalk suppression are prioritized.

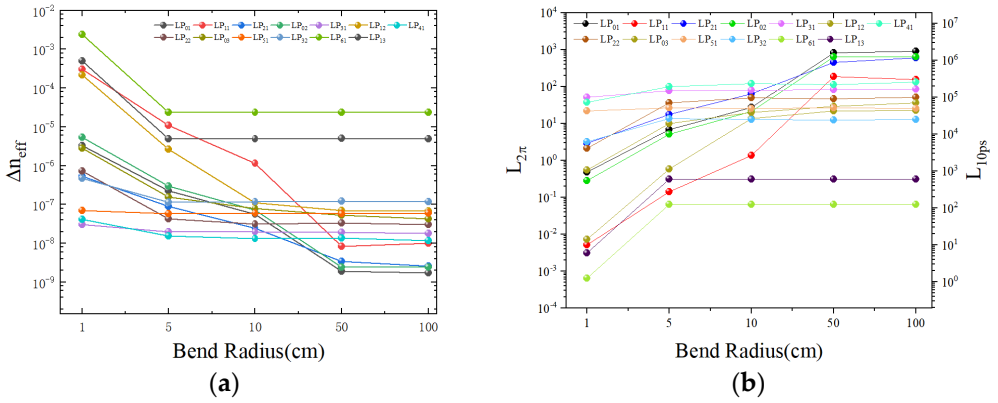


Figure 13. (**a**) Effective refractive index differences; (**b**) $\mathbf{L_{2\pi}}$ and $\mathbf{L_{10ps}}$ versus bend radius for the CRA 13–LP mode fiber.

The primary optical characteristics of the optimized CRA 13-LP mode fiber at 1550 nm is summarized in Table 2. Compared to the RA 11-LP mode group fiber, the Min | A_{eff} | of the CRA fiber slightly decreases to 131 μm^2; however, it remains well above 100 μm^2. Following the theoretical framework in Equation (5), the nonlinear coefficient γ for the CRA structure is calculated to be 0.74 $W^{-1} \times km^{-1}$ at 1550 nm. This low γ value is particularly crucial for CRA fibers as it minimizes the nonlinear phase noise that could otherwise lead to the crosstalk between degenerate OAM modes, thereby ensuring the purity and stability of mode division multiplexing over long distances, and effectively mitigating nonlinear impairments. The Min | Δn_{eff} | is maintained at 0.55×10^{-3}, providing sufficient suppression of inter-modal crosstalk (IM-XT) despite the increased mode density. Although the differential group delay (DGD) naturally scales with the number of supported modes, it is strictly confined within 42 ps/m. Furthermore, the chromatic dispersion is capped at 45 ps/(nm $\times$ km). Notably, the confinement loss is approximately 10^{-12} dB/km, ensuring excellent signal confinement, although actual attenuation would be dominated by material scattering and absorption (typically 0.2 dB/km). Similarly, the CRA-FMF maintains a robust Min | Δn_{eff} | of 0.55×10^{-3}, providing a nearly six-fold safety margin above the 10^{-4} threshold. This ensures stable mode isolation and high fabrication tolerance even with the increased mode density, effectively suppressing inter-mode crosstalk during practical manufacturing.

Table 2. Characteristics of the optimized CRA 13-LP mode fiber at 1550 nm.

	LP_{01}	LP_{11}	LP_{21}	LP_{02}	LP_{31}	LP_{12}	LP_{41}
$n_{eff}(\times 1)$	1.4588	1.4579	1.4562	1.4548	1.4542	1.4533	1.4520
Min$\left\|\Delta n_{eff}\right\|(\times 10^{-3})$				0.55			
$A_{eff}(\mu m^2)$	255	191	225	257	243	238	22.7
DGD vs. LP_{01} (ps/m)		3.2	8.8	13.6	15.4	18.6	22
Dispersion [ps/(nm·km)]	9.85	17.16	14.98	9.62	44.2	12.88	16.57
Limited Loss (10^{-12} dB/km)	0.257	0.001	0.278	0.212	0.170	0.105	0.791
	LP_{22}	LP_{03}	LP_{51}	LP_{32}	LP_{61}	LP_{13}	
$n_{eff}(\times 1)$	1.4513	1.4502	1.4497	1.4487	1.4470	1.4464	
Min$\left\|\Delta n_{eff}\right\|(\times 10^{-3})$				0.55			
$A_{eff}(\mu m^2)$	232	131	221	217	212	165	
DGD vs. LP_{01} (ps/m)	24.9	28.7	30.6	33.8	39.3	41.3	
Dispersion [ps/(nm·km)]	28.39	26.23	9.72	42.7	24.78	40.64	
Limited Loss (10^{-12} dB/km)	0.213	1.102	0.041	0.003	0.340	0.577	

4.3. Performance Comparison and Discussion

Table 3 presents a quantitative comparison between our designs and previously reported few-mode fibers. While the RA-FMF supports 11 LP mode groups with a Min | Δn_{eff} | of 0.78 × 10^{-3}, the optimized CRA-FMF expands the capacity to 13 LP mode groups (46 modes). Despite the increased mode density, the CRA-FMF maintains 0.78 × 10^{-3} of 0.55 × 10^{-3}, effectively suppressing inter-mode power transfer and crosstalk to enable low-complexity MIMO equalization. Furthermore, the CRA-FMF achieves a Min | A_{eff} | of 131 μm^2, which is vital for mitigating nonlinear effects in long-haul transmission. Compared to the four LP mode design in [48] with a DMD of 13.45 ns/km, our CRA-FMF provides a 3.8-fold capacity increase while maintaining a manageable DMD of 44.2 ns/km. These results confirm that the graded concave profile superiorly balances high spatial efficiency, robust coupling suppression, and nonlinear tolerance.

Table 3. Performance comparison of various weakly coupled fiber designs in terms of mode capacity and index difference.

Reference	Structure	Number of Spatial Modes	Min | Δn_{eff} | ($\times 10^{-3}$)	Min $\left\|A_{eff}\right\|$ (μm^2)	Max | DGD | (ps/m)
[44]	Ellipse-assisted	10	0.32	-	-
[46]	Ring-core	6	0.08	-	-
[52]	Ring-assisted	12	1.2	532	-
[53]	High-index-ring	12	2.01	42	13.45
This work	Ring-assisted	38	0.78	161	36.5
This work	Concentric-ring-assisted	46	0.55	131	44.2

Furthermore, the proposed CRA-FMF offers significant advantages for practical system integration and selective mode excitation in MDM networks. The fiber's large Min | Δn_{eff} | of 0.55 × 10^{-3} ensures strong suppression of inter-modal crosstalk, providing high modal stability during long-haul transmission. In a typical communication link, independent data streams from a single-mode fiber (SMF) array can be converted and coupled into the specific supported modes of the CRA-FMF using multiplexing devices such as photonic lanterns, mode-selective couplers (MSCs), or free-space mode sorters. The performance of these excitation devices is highly dependent on phase-matching conditions. Our design's superior Δn_{eff} ensures a sharp phase-matching response, which effectively suppresses unwanted coupling to adjacent modes and enhances mode purity. At the receiver end, the spatial channels are demultiplexed and recovered using low-complexity MIMO processing.

Combined with its manageable DMD and large Min | A_{eff} |, the CRA-FMF demonstrates strong potential for seamless integration into existing weakly coupled MDM systems.

5. Conclusions

We have proposed and numerically demonstrated an RA fiber supporting 11 LP mode groups and a CRA fiber supporting 13 LP mode groups. By introducing a high refractive index ring to overlap with the LP_{22} mode, the effective refractive index of the LP_{22} mode is largely improved. We have successfully designed the RA 11-LP mode fiber with Min | Δn_{eff} | $= 0.78 \times 10^{-3}$, which is almost the same as the SI-4 mode fiber. On this basis, we designed the CRA 13-LP mode fiber in the same way. Based on the existing first RA structure, a second concentric RA structure was added. The second RA structure enhances the effective refractive index of LP_{61} by overlapping with the LP_{61} mode. Furthermore, Min | Δn_{eff} | $= 0.55 \times 10^{-3}$ and Min | A_{eff} | $= 131\ \mu m^2$ for the CRA 13-LP mode fiber, and the effective refractive index is stable for all LP modes within the C band. Through multiple RA structures, it is expected to achieve a CRA fiber that can support more LP modes and improve the transmission capacity of the fiber.

Regarding the practical feasibility, the CRA fiber can be precisely realized using modern MCVD or PCVD techniques, where dopant flow rates are finely tuned to achieve the required 10^{-4} refractive index resolution. The scalability of this multi-ring geometry allows for flexible adaptation to higher-order OAM mode transmission or large-mode-area applications by proportionally adjusting the radial dimensions. Future work will focus on experimental verification, including preform fabrication and characterization of transmission loss and modal crosstalk, to further validate its application prospects in high-capacity optical communications and advanced sensing.

Author Contributions: Conceptualization, Y.L. and C.Z.; methodology, Y.L., S.M. and C.Z.; software, C.Z. and X.Z.; validation, C.Z.; formal analysis, Y.L., X.Z. and C.Z.; investigation, C.Z.; data curation, C.Z.; writing—original draft preparation, C.Z.; writing—review and editing, H.X., J.Z., Y.L. and S.M.; visualization, H.X., J.Z. and C.Z.; supervision, Y.L. and S.M.; project administration, Y.L. and S.M.; funding acquisition, X.Z. and Y.L. All authors have read and agreed to the published version of the manuscript.

Funding: This work was supported by the National Natural Science Foundation of China (62405233), the Opening Project of Modern Precision Measurement and Laser Non-destructive Testing Key Laboratory of Higher Education in Fujian Province (Putian University, Grants No. XKA202505), and the Jiangsu Funding Program for Excellent Postdoctoral Talent (2025ZB101).

Data Availability Statement: All data, theory details, and simulation details that support the findings of this study are available from the corresponding authors upon reasonable request.

Conflicts of Interest: Author Xi Zhang was employed by the company Jiangsu Alpha Optic-Electric Technology Co., Ltd. Author Haixuan Xu was employed by the company China Mobile Information Technology Co., Ltd. The remaining authors declare that the research was conducted in the absence of any commercial or financial relationships that could be construed as a potential conflict of interest.

References

1. Essiambre, R.; Kramer, G.; Winzer, P.J.; Foschini, G.J.; Goebel, B. Capacity limits of optical fiber networks. *J. Light. Technol.* **2010**, *28*, 662–701. [CrossRef]
2. Liang, Y.; Wang, H.; Liu, J.; Wang, J. Experimental demonstration of visualized multi-core fiber coupling alignment system for inter-core cross talk measurement. *Opt. Lett.* **2022**, *47*, 3071–3074. [CrossRef]
3. Wang, Y.; Yang, C.; Wang, Y.; Chi, N. Gigabit polarization division multiplexing in visible light communication. *Opt. Lett.* **2014**, *39*, 1823–1826. [CrossRef]
4. Dong, P. Silicon photonic integrated circuits for wavelength-division multiplexing applications. *IEEE J. Sel. Top. Quant.* **2016**, *22*, 370–378. [CrossRef]

5. Hamilton, S.A.; Robinson, B.S.; Murphy, T.E.; Savage, S.J.; Ippen, E.P. 100 Gb/s Optical Time-Division Multiplexed Networks. *J. Light. Technol* **2002**, *20*, 2086. [CrossRef]
6. Richardson, D.J.; Fini, J.M.; Nelson, L.E. Space-division multiplexing in optical fibres. *Nat. Photonics* **2013**, *7*, 354–362. [CrossRef]
7. Ma, Z.; Ramachandran, S. Propagation stability in optical fibers: Role of path memory and angular momentum. *Nanophotonics* **2021**, *10*, 209–224. [CrossRef]
8. Liang, Y.; Cao, S.; Liu, L.; Liu, F.; Yin, X.; Lv, P.; Zhang, Y.; Zou, Y.; Fang, L.; Zheng, S.; et al. Coherent detector for the non-separability measurement of vectorial structured light. *Light Sci. Appl.* **2025**, *14*, 343. [CrossRef]
9. Ingerslev, K.; Gregg, P.; Galili, M.; Da Ros, F.; Hu, H.; Bao, F.; Castaneda, M.A.U.; Kristensen, P.; Rubano, A.; Marrucci, L.; et al. 12 mode, WDM, MIMO-free orbital angular momentum transmission. *Opt. Express* **2018**, *26*, 20225–20232. [CrossRef]
10. Li, G.; Bai, N.; Zhao, N.; Xia, C. Space-division multiplexing: The next frontier in optical communication. *Adv. Opt. Photonics* **2014**, *6*, 413–487. [CrossRef]
11. Puttnam, B.J.; Rademacher, G.; Luís, R.S. Space-division multiplexing for optical fiber communications. *Optica* **2021**, *8*, 1186–1203. [CrossRef]
12. Lu, K.; Chen, Z.; Chen, H.; Zhou, W.; Zhang, Z.; Tsang, H.K.; Tong, Y. Empowering high-dimensional optical fiber communications with integrated photonic processors. *Nat. Commun.* **2024**, *15*, 3515. [CrossRef] [PubMed]
13. Ma, Z.; Kristensen, P.; Ramachandran, S. Scaling information pathways in optical fibers by topological confinement. *Science* **2023**, *380*, 278–282. [CrossRef] [PubMed]
14. Bozinovic, N.; Yue, Y.; Ren, Y.; Tur, M.; Kristensen, P.; Huang, H.; Willner, A.E.; Ramachandran, S. Terabit-Scale Orbital Angular Momentum Mode Division Multiplexing in Fibers. *Science* **2013**, *340*, 1545–1548. [CrossRef]
15. Wang, J. Advances in communications using optical vortices. *Photonics Res.* **2016**, *4*, B14–B28. [CrossRef]
16. Liang, Y.; Wang, H.; Zhang, X.; Ai, J.; Ma, Z.; Ramachandran, S.; Wang, J. Reconfigurable structured light generation and its coupling to air–core fiber. *Adv. Photonics Nexus* **2023**, *2*, 36015. [CrossRef]
17. Wang, F.; Gao, R.; Li, Z.; Liu, J.; Cui, Y.; Xu, Q.; Pan, X.; Zhu, L.; Wang, F.; Guo, D.; et al. OAM mode-division multiplexing IM/DD transmission at 4.32 Tbit/s with a low-complexity adaptive-network-based fuzzy inference system nonlinear equalizer. *Opt. Lett.* **2024**, *49*, 430–433. [CrossRef]
18. Liang, Y.; Xi, T.; Cao, S.; Liu, L.; Liu, F.; Wan, Z.; Wang, J.; Shao, X. Spatiotemporal vectorial structured light that dynamically varies on higher-order Poincaré sphere. *Opt. Express.* **2024**, *32*, 28413–28428. [CrossRef]
19. Cao, S.; Ruan, Z.; Ren, W.; Qin, S.; Yin, X.; Liu, L.; Liang, Y.; Xu, H. Tailoring Perfect Optical Vortex Combs Based on Diffractive Neural Networks. *Laser Photonics Rev.* **2025**, *20*, e2383. [CrossRef]
20. Mojaver, K.R.; Safaee, S.M.R.; Morrison, S.S.; Liboiron-Ladouceur, O. Recent Advancements in Mode Division Multiplexing for Communication and Computation in Silicon Photonics. *J. Light. Technol.* **2024**, *42*, 7860–7870. [CrossRef]
21. Liang, Y.; Hu, X.; Wang, Q.; Wang, J. Tailoring optical vortex beams based on diffractive neural networks for high-quality ring-core fiber coupling. *Opt. Lett.* **2025**, *50*, 3788–3791. [CrossRef]
22. Gregg, P.; Kristensen, P.; Ramachandran, S. Conservation of orbital angular momentum in air-core optical fibers. *Optica* **2015**, *2*, 267–270. [CrossRef]
23. Bushuev, D.; Arnon, S. Analysis of the performance of a wireless optical multi-input to multi-output communication system. *J. Opt. Soc. Am.* **2006**, *23*, 1722–1730. [CrossRef] [PubMed]
24. Willner, A.E.; Song, H.; Zou, K.; Zhou, H.; Su, X. Orbital angular momentum beams for high-capacity communications. *J. Light. Technol.* **2022**, *41*, 1918–1933. [CrossRef]
25. Liu, J.; Zhang, J.; Liu, J.; Lin, Z.; Li, Z.; Lin, Z.; Zhang, J.; Huang, C.; Mo, S.; Shen, L. 1-Pbps orbital angular momentum fibre-optic transmission. *Light Sci. Appl.* **2022**, *11*, 202.
26. Yue, Y.; Yan, Y.; Ahmed, N.; Yang, J.; Zhang, L.; Ren, Y.; Huang, H.; Birnbaum, K.M.; Erkmen, B.I.; Dolinar, S. Mode properties and propagation effects of optical orbital angular momentum (OAM) modes in a ring fiber. *IEEE Photonics J.* **2012**, *4*, 535–543.
27. Sillard, P.; Bigot-Astruc, M.; Molin, D. Few-mode fibers for mode-division-multiplexed systems. *J. Light. Technol.* **2014**, *32*, 2824–2829. [CrossRef]
28. Wang, J.; Zhang, X. Orbital angular momentum in fibers. *J. Light. Technol.* **2022**, *41*, 1934–1962. [CrossRef]
29. Geng, W.; Fang, Y.; Bao, C.; Pan, Z.; Yue, Y. Emission of five OAM dispersive waves in dispersion-engineered double-ring core fiber. *Sci. Rep.* **2024**, *14*, 8474. [CrossRef]
30. Zhao, W.; Wang, Y.; Ren, H.; Geng, W.; Liu, Y.; Pan, Z.; Yue, Y. Recent advances in ring-core fiber for orbital-angular-momentum-based mode-division multiplexing. *Opt. Commun.* **2025**, *591*, 132091. [CrossRef]
31. Wang, G.; Zhang, J.; Zhang, H.; Wang, F.; Yan, X.; Zhang, X.; Li, S.; Cheng, T. A low crosstalk multi-core few-mode fiber with composite refractive index profile and air-hole embedded trench assistance. *Opt. Commun.* **2021**, *499*, 127258.
32. Zhang, J.; Zhu, J.; Liu, J.; Mo, S.; Zhang, J.; Lin, Z.; Shen, L.; Zhang, L.; Luo, J.; Liu, J. Accurate mode-coupling characterization of low-crosstalk ring-core fibers using integral calculation based swept-wavelength interferometry measurement. *J. Light. Technol.* **2021**, *39*, 6479–6486.

33. Zhang, X.; Wang, J. Design of Multilayered Ring-Core Fiber With Low-Level Inter-Group Crosstalk. *IEEE J. Quantum Elect.* **2023**, *59*, 6800208. [CrossRef]
34. Sillard, P.; Bigot-Astruc, M.; Boivin, D.; Maerten, H.; Provost, L. Few-Mode Fiber for Uncoupled Mode-Division Multiplexing Transmissions. In *37th European Conference and Exposition on Optical Communications*; Optica Publishing Group: Geneva, Switzerland, 2011.
35. Ma, L.; Jiang, S.; Du, J.; Yang, C.; Tong, W.; He, Z. Ring-Assisted 7-LP-Mode Fiber with Ultra-Low Inter-Mode Crosstalk. In Proceedings of the 2016 Asia Communications and Photonics Conference (ACP), Wuhan, China, 2–5 November 2016.
36. Zhu, G.; Hu, Z.; Wu, X.; Du, C.; Luo, W.; Chen, Y.; Cai, X.; Liu, J.; Zhu, J.; Yu, S. Scalable mode division multiplexed transmission over a 10-km ring-core fiber using high-order orbital angular momentum modes. *Opt. Express* **2018**, *26*, 594–604. [CrossRef]
37. Zhu, L.; Zhu, G.; Wang, A.; Wang, L.; Ai, J.; Chen, S.; Du, C.; Liu, J.; Yu, S.; Wang, J. 18 km low-crosstalk OAM + WDM transmission with 224 individual channels enabled by a ring-core fiber with large high-order mode group separation. *Opt. Lett.* **2018**, *43*, 1890–1893. [CrossRef] [PubMed]
38. Ramachandran, S.; Gregg, P.; Kristensen, P.; Golowich, S.E. On the scalability of ring fiber designs for OAM multiplexing. *Opt. Express* **2015**, *23*, 3721–3730. [CrossRef] [PubMed]
39. Demas, J.; Hary, M.; Genty, G.; Ramachandran, S. Optimization and realignment of OAM mode excitation in ring-core optical fibers using machine learning. *Opt. Lett.* **2024**, *49*, 5003–5006. [CrossRef]
40. Gulistan, A.; Ghosh, S.; Ramachandran, S.; Rahman, B.M.A. Efficient strategy to increase higher order inter-modal stability of a step index multimode fiber. *Opt. Express* **2017**, *25*, 29714–29723. [CrossRef]
41. Gulistan, A.; Ghosh, S.; Rahman, B. Enhancement of modal stability through reduced mode coupling in a few-mode fiber for mode division multiplexing. *OSA Continuum* **2018**, *1*, 309–319. [CrossRef]
42. Jiang, S.; Ma, L.; Zhang, Z.; Xu, X.; Wang, S.; Du, J.; Yang, C.; Tong, W.; He, Z. Design and characterization of ring-assisted few-mode fibers for weakly coupled mode-division multiplexing transmission. *J. Light. Technol.* **2018**, *36*, 5547–5555.
43. He, Z.; Du, J.; Chen, X.; Shen, W.; Huang, Y.; Wang, C.; Xu, K.; He, Z. Machine learning aided inverse design for few-mode fiber weak-coupling optimization. *Opt. Express* **2020**, *28*, 21668–21681. [CrossRef] [PubMed]
44. Jin, X.; Gomez, A.; Shi, K.; Thomsen, B.C.; Feng, F.; Gordon, G.S.D.; Wilkinson, T.D.; Jung, Y.; Kang, Q.; Barua, P.; et al. Mode Coupling Effects in Ring-Core Fibers for Space-Division Multiplexing Systems. *J. Light. Technol.* **2016**, *34*, 3365–3372. [CrossRef]
45. Simović, A.; Djordjevich, A.; Savović, S. Influence of depth of intermediate layer on optical power distribution in W-type optical fibers. *Appl. Opt.* **2012**, *51*, 4896–4901. [CrossRef] [PubMed]
46. Brunet, C.; Ung, B.; Wang, L.; Messaddeq, Y.; LaRochelle, S.; Rusch, L.A. Design of a family of ring-core fibers for OAM transmission studies. *Opt. Express* **2015**, *23*, 10553–10563. [CrossRef]
47. Simović, A.; Drljača, B.; Savović, S.; Djordjevich, A.; Min, R. Investigation of bandwidth in multimode graded-index plastic optical fibers. *Opt. Express* **2021**, *29*, 29587–29594. [CrossRef]
48. Zhang, X.; Chen, S.; Wang, J. Weakly guiding graded-index ring-core fiber supporting 16-channel long distance mode division multiplexing systems based on OAM modes with low MIMO-DSP complexity. *Opt. Express* **2022**, *30*, 35828–35839. [CrossRef]
49. Song, Y.; Zheng, J.; Pei, L.; Huang, J.; Wang, J.; Ning, T.; Li, J.; Bai, B. Design and characteristics of ellipse-assisted ring-core fiber for space division multiplexing. *Opt. Fiber Technol.* **2022**, *72*, 102984. [CrossRef]
50. Yan, Z.; Sun, Q.; Wang, C.; Sun, Z.; Mou, C.; Zhou, K.; Liu, D.; Zhang, L. Refractive index and temperature sensitivity characterization of excessively tilted fiber grating. *Opt. Express* **2017**, *25*, 3336–3346. [CrossRef]
51. Liang, J.; Qiao, G.; Wei, J.; Li, J.; Yang, Y.; Xu, Z.; Liu, L.; Wang, S.; Wu, Q.; Hu, W. Micro-Bending Influence on Mode-Dependent Loss. In Proceedings of the 2023 IEEE 15th International Conference on Advanced Infocomm Technology (ICAIT), Hefei, China, 13–16 October 2023; pp. 203–206.
52. Lu, G.; Liu, S.; Lv, D.; Chen, M.; Zhang, Z. Design of ring-assisted few-mode fiber with low loss for improved mode-division multiplexing. *Laser Phys.* **2021**, *31*, 105101. [CrossRef]
53. Zhang, J.; Wang, G.; Zhang, H.; Wang, F.; Yan, X.; Zhang, X.; Li, S.; Cheng, T. A Weakly-Coupled Few-Mode Optical Fiber With a Graded Concave High-Index-Ring. *IEEE Photonics J.* **2021**, *13*, 7200710.

Disclaimer/Publisher's Note: The statements, opinions and data contained in all publications are solely those of the individual author(s) and contributor(s) and not of MDPI and/or the editor(s). MDPI and/or the editor(s) disclaim responsibility for any injury to people or property resulting from any ideas, methods, instructions or products referred to in the content.